Conditioning Electrical Impedance Mammography System

Ali Zarafshani*[a,c,d], Thomas Bach[b], Chris R. Chatwin[a] , Shanshan Tang[c], Liangzhong Xiang[c] , and Bin Zheng[d]

[a] Biomedical Research Group, Department of Eng. and Design, School of Eng. and Informatics, University of Sussex, UK, BN19QT

[b] Sensatech Research Ltd, Brighton, UK, BN2 0GP

[c] TRUE Lab, School of Electrical and Computer Eng., University of Oklahoma, Norman, OK, 15213, USA

[d] CAD Lab, Stephenson Cancer Research Center, School of Electrical and Computer Eng., University of Oklahoma, Norman, OK, 15213, USA

* Corresponding author
Ali Zarafshani, Ph.D.,
101 David L Boren Blvd. Suite 1001
School of Electrical and Computer Engineering,
University of Oklahoma,
Norman, OK 73019
Email: A.Zarafshani@ou.edu (AZ)

ABSTRACT

A multi-frequency Electrical Impedance Mammography (EIM) system has been developed to evaluate the conductivity and permittivity spectrums of breast tissues, which aims to improve early detection of breast cancer as a non-invasive, relatively low cost and label-free screening (or pre-screening) method. Multi-frequency EIM systems typically employ current excitations and measure differential potentials from the subject under test. Both the output impedance and system performance (SNR and accuracy) depend on the total output resistance, stray and output capacitances, capacitance at the electrode level, crosstalk at the chip and PCB levels. This makes the system design highly complex due to the impact of the unwanted capacitive effects, which substantially reduce the output impedance of stable current sources and bandwidth of the data that can be acquired. To overcome these difficulties, we present new methods to design a high performance, wide bandwidth EIM system using novel second generation current conveyor operational amplifiers based on a gyrator (OCCII-GIC) combination with different current excitation systems to cancel unwanted capacitive effects from the whole system. We reconstructed tomography images using a planar E-phantom consisting of an RSC circuit model, which represents the resistance of extra-cellular (R), intra-cellular (S) and membrane capacitance (C) of the breast tissues to validate the performance of the system. The experimental results demonstrated that an EIM system with the new design achieved a high output impedance of $\mathbf{10M\Omega}$ at 1MHz to at least $\mathbf{3M\Omega}$ at 3MHz frequency, with an average SNR and modelling accuracy of over 80dB and 99%, respectively.

***Index Terms*— Biomedical imaging equipment and instrument, screening and prescreening modality, breast cancer detection, electrical impedance tomography, bio-impedance current source, and electrical impedance mammography.**

1. INTRODUCTION

Electrical Impedance Spectroscopy (EIS) [1-3] or multi-frequency Electrical Impedance Tomography (EIT) [4-6] systems were designed and used to measure extensive electrical properties based on the conductivity and permittivity of the biological tissues, which are quite different from other conventional medical imaging modalities that mostly used to detect or describe tissue density, stiffness, and other physical features. Multi-frequency EIT provides a new alternative or supplementary approach to help improve diagnosis of breast cancer based on the differentiation of dielectric properties of biological tissues [7], as there is a significant difference in dielectric properties between the normal and malignant tissues [8,9]. The EIT technique has unique several advantages such as: non-invasive, relatively inexpensive, no-hazardous attachments, non-ionizing radiation, label-free, possibility of repeated use without any side effects, and capability of quantitative measurement of electrical characteristics [10,11]. Therefore, it is proposed as a new potential breast cancer screening or pre-screening method to detect malignant tumors at early stage [12,13]. In this regard, it is suggested to call it "Electrical Impedance Mammography (EIM)" [14-17].

An EIM system includes a number of software and hardware subsystems consisting of analogue and digital elements that are usually developed together [18-20]. Specifically, an EIM system consists of a signal generator, voltage-to-current (V/I) convertors, drive and receive multiplexers (MUXs) in case of single source topology, channel switching control with calibration circuits, differential voltage amplifiers, and DSP components to demodulate and find "in-phase" and "quadrature" of the transfer voltage measurements at different frequency points leading to a breast impedivity image reconstruction (IR), the EIM structure is shown in Fig. 1.

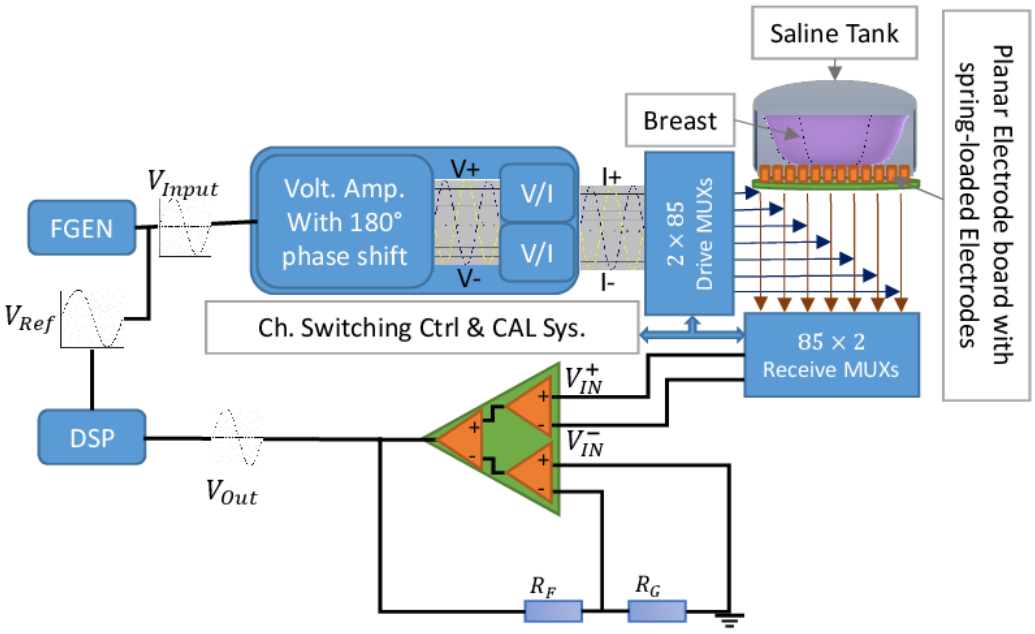

Fig. 1. Overview of the single source Sussex EIM system regarding the Sussex 85 planar electrode structure

For reconstructing the impedivity image of a breast under test, it is required to employ a current excitation and the data acquisition system (DAS) to measure different potentials at multi-frequency points [21]. Indeed, on the subject of injecting current, in order to achieve high measurement precision, it is important that the current injection circuits have a high output impedance over the required frequency bandwidth [22]. This will deliver a high-performance system with improved spatial resolution to measure electrical impedance properties of biological tissues [23]. The change in electrical properties of a small region of tissue can be observed over a frequency range of interest [24]. These changes can provide significant information about the structure and composition of the tissue [25-27]. Since tissue electrical properties are determined by their resistive and capacitive characteristics, the measured values depend upon the conductivity σ and permittivity ε, which quantifies the tissue's ability to permit storage of electric energy [28]. Therefore, these high-frequency measurements are vital for intracellular impedance imaging because membranes of cells block the current flowing to inside the cells at low frequency [29].

Multi-frequency EIM systems typically employ current excitations and measure differential potentials from the subject under test. Both the output impedance and system performance (SNR and accuracy) depend on the total output resistance, stray and output capacitances, capacitance at the electrode level, crosstalk at the chip and PCB levels. This makes the design of system highly complex due to the impact of the unwanted capacitance, which substantially reduces the output impedance of stable current sources and bandwidth of the required data. In order to overcome this difficulty, the objective of this study is to apply a new EIM system design method and test whether the new system can produce significantly higher contrast in generating EIM images. To report our study methods and results, this article is organized as follows. We first provide a theoretical description of the voltage and current-mode source topologies as the main part of the hardware subsystem. Next, we propose a current conveyor structure by application of a gyrator to eliminate the current excitation limitations, and its development is followed by experimental tests to show the potential enhancement of the detected signals. We also build an Electric phantom (E-phantom) with an RSC circuit model to simulate breast tissue electrical properties. Then, we conducted experiments to test the potential enhancement of the detected or measured EIM signals from the breast phantom. The results are presented and discussed in the last section of this article.

2. MATERIALS AND METHODS

2.1 Current excitation system

The most recent technique for developing clinical and physiological applications of EIT systems is based on applying a known value of low amplitude current between 0.1–2mA. It is injected into the subject at different frequencies. Consequently, measuring the resulting multi-frequency potentials around 10 kHz up to a few MHz in order to produce an impedance based image of the biological tissue sample. This design meets standard IEC 60601-1 for biomedical systems in which the maximum amount of current injection must be limited to 10mA above 100 kHz. The current source topologies are commonly employed instead of voltage sources, due to advantages including predictability of constant current, high output impedance and low noise advantages. For example, current sources were utilized by Kyung Hee (IIRC); Oxford Brookes (OXBACT5); Rensselaer (ACT4); Sheffield (Mk3.5); UCL (Mk2.5&1b), and also the Leicester group (Mk3) [11,22,30-35] in developing their EIT or EIS systems.

The key factor or evaluation index in assessing performance and reliability of multi-frequency systems is signal-to-noise ratio (SNR) and its accuracy [36-39], which are directly affected by the output impedance of the current excitation system when measuring the voltage between two points of the sample tissue. In reality, the output impedance of the current source is not infinite. Since the current excitation system is affected by output capacitance C_O, and output resistance R_O. The output capacitance effects generated by the current source circuitry and extra capacitance that exists in electrical components in the output signal path such as MUXs, capacitances on the PCB copper tracks, which carry the output signal to other copper areas. These capacitances represented by output capacitance of the source C_O, stray capacitance C_{Stray} are in parallel with the load impedance Z_{load} and output resistance R_O, as shown in Fig. 2. These unwanted capacitances can significantly reduce the output impedance amplitude of the current excitation system and introduce additional phase shifts at high frequencies.

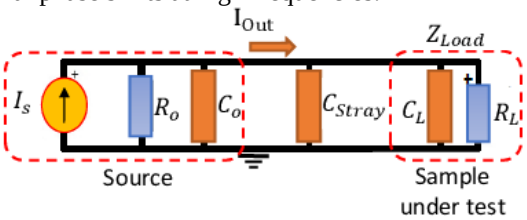

Fig. 2. Real current source circuit with stray capacitances

The most popular current source topologies that are employed in bio-impedance excitation systems are Howland based current source, mirror current source, Wien Bridge circuit, V/I sources and current conveyor source, however, each has advantages and disadvantages [40-44]. In order to improve system performance a new Sussex EIM system was developed. In this study, the improved Howland current source (voltage-mode current source) and the current conveyor current source (current-mode current source) will be employed more thoroughly and used as the two main current excitation topologies for bio-impedance measurement systems. The motivation of selecting these two current sources is due to their potential advantages in bandwidth, precision of current pattern at multi-frequency range for various loads and complexity of circuitry, which is results in greater stability and reproducibility of the measured output signals.

2.2 Voltage-mode current source

Bradford Howland at MIT developed the basic Howland current source [45]. The Howland current source is a circuit that provides an AC or DC current source with a high output impedance and wide bandwidth range [41]. The "Improved" Howland source consisting of 5 resistors, where R_4 in the Howland source is divided into R_{4a} and R_{4b} and the output node of the current source is placed between these two resistors. The

schematic diagram of the improved Howland current source limited by the existence of the unwanted stray capacitance in parallel to the load impedance is shown in Fig. 3.

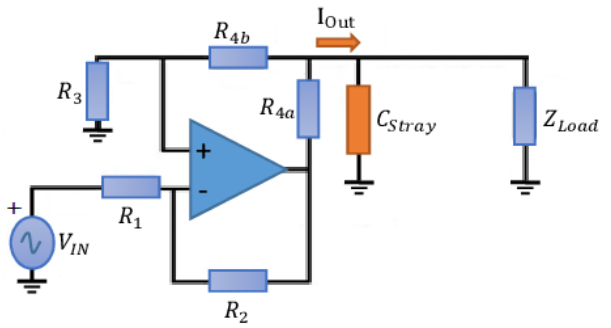

Fig. 3. The improved Howland current source

In this topology, the source output resistance (R_O) ideally becomes infinite when the ratio R_1/R_2 is equal to $R_3/(R_{4a}+R_{4b})$. It means, if we choose R_1 equals R_2, then R_3 must also equal $(R_{4a}+R_{4b})$ to yield the maximum output resistance. However, since op amp practical limitations of upper bandwidth and resistors are available in different tolerances (banding B, C, D, F, G, J, K, and M with tolerance of 0.1–20%) the above perfect ratio is never met, therefore, these limitations can cause alteration in the output impedance of the current source [41]. As reported by previous studies [40-44], all current source circuits at some frequency suffer from a reduction of current into the injecting pads and a change in phase. Parasitic capacitance from the PCB tracks and in any multiplexers or cross-point switches will cause a further drop in the output impedance at the injecting pads. Thus, a capacitance elimination circuit can improve the total output impedance and bandwidth of any of these systems.

2.3 Current-mode current source

The second most common technique to make an electrical current generator is the "current mirror technique" as utilized by many research groups [46-48]. It can produce a constant current with high output impedance at high frequency based on the current-mode structure using "current conveyor" a three-terminal analogue structure. Sedra and Smith introduced the current conveyor (CC) as an active component [49], which can provide many signal processing functions such as current integrator, current differentiator, voltage or current amplifier, V/I convector etc. Since it is an active component, thus, it will be more stable and suitable for integrated implementation. The current conveyor simplifies circuit design as a current feedback op amp and can be implemented as an op amp with higher voltage gain, which is not limited by the conventional voltage feedback op amp having a standard gain bandwidth [50,51]. Based on the second generation of current conveyer (CCII) [52], if a voltage is applied to the high impedance non-inverting input (Y), it is expected that the same voltage appears on the low impedance inverting input (X), which means $V_X=V_Y$, while the current applied to the inverting input node (X) is conveyed by mirrors to the Trans-impedance output node (T_Z). Based on the circuit shown in Fig. 4 (a), T_Z and Y nodes are high impedance and X node is low impedance, since the current in non-inverting node (Y) is ideally equal to zero.

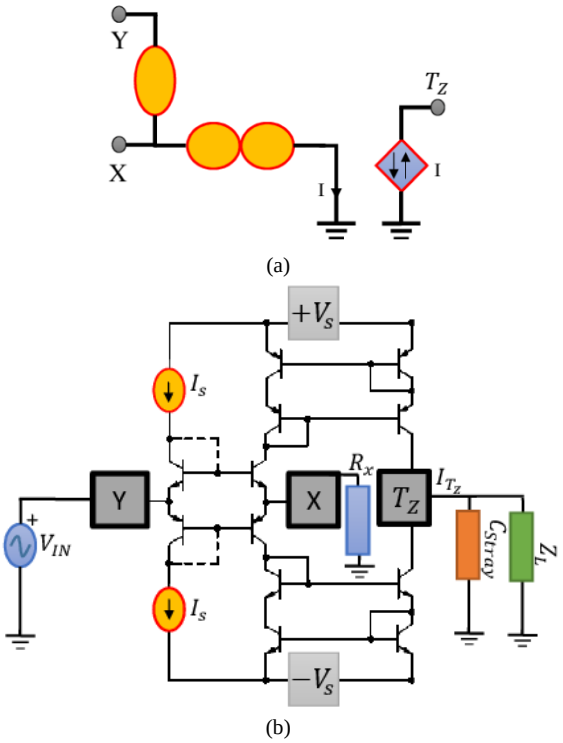

Fig. 4. (a) Simplified current model of CCII, (b) Simplified the transistor schematic of the CCII in the functionality of current source. The X input node is connected to ground via a resistor (R_x) thus the current mirrored from the X node to T_Z node based $V_Y=V_X$ and $I_Y=0$.

In regard to current conveyor behavior, Fig. 4 (b) shows the transistor current source schematic diagram in which T_Z node generates the output current with high impedance, when the X (input node) is connected to ground through a resistor (R_X). A simplified transistor schematic of the CCII shows the differences between the simple conventional voltage feedback op amp and current conveyor. However, in an actual implementation, the voltage at X node (V_X) is not equal to that at Y node (V_Y). Thus, current at Y node is not equal to that at T_Z node where the characteristic functions are given by, $V_X=\beta V_Y$, $I_Y=0$ and $I_{TZ}=\pm\alpha I_X$. The output current will then be calculated as:

$$I_{TZ} = \alpha\beta \frac{V_{in}}{R_X} \qquad 1$$

However, in practice the effective output capacitance of the current source and the parasitic capacitances create a total grounded capacitance (denoted by stray capacitance), which makes it impractical to produce an EIM system operating at high frequency. Therefore, stray capacitance is the key issue affecting the output impedance of the current excitation systems. It reduces the useful frequency bandwidth of the system. Thus, for utilizing the current excitation system at high frequency, it is necessary to cancel unwanted capacitive effects. Therefore, in the following section, we propose a new method based on active component structures for multi-frequency systems.

2.4 Cancellation of the unwanted capacitive effects

The generalized impedance converter (GIC) can be used in many functionalities, i.e. programmable impedance in the synthesis of a filter design, oscillator design, analogue phase

shifters and cancellation of parasitic elements. These applications use combinations of passive impedances, op amps, Trans-conductance amplifiers and current conveyor to synthesize programmable impedances [53-56].

The advent of the GIC in parallel with the current source has provided a way to reduce the capacitive effect at high frequency. It creates an RLC circuit with an LC resonant condition. The LC resonance occurs when both inductive and total capacitive reactants are equal at a particular frequency. Although, the conventional GIC is already proposed based on two op amps and five passive components utilized in ACT4 and KHU Mark1 EIT systems to provide a grounded inductance. However, because of using five dependent passive components, several digital-pots structure and op amp limitations, it is impractical to produce a multi-frequency EIT system operating at high frequency.

Therefore, a new active gyrator technique for cancellation of the parasitic elements in EIM excitation sources is presented to cancel the effects of both stray and output capacitances of the current source through a compensating inductance. The desired technique is based on a gyrator structure using operational two stages of CCIIs (OCCIIs). The proposed combination of OCCII as a GIC (here is called OCCII-GIC structure) is shown in Fig. 5 [57-62]. An inductance synthesized by using an OCCII-GIC structure in parallel with the current source is improved by incorporating a tuning system. This maximizes output impedance and eliminates the stray capacitance in multi-frequency operation.

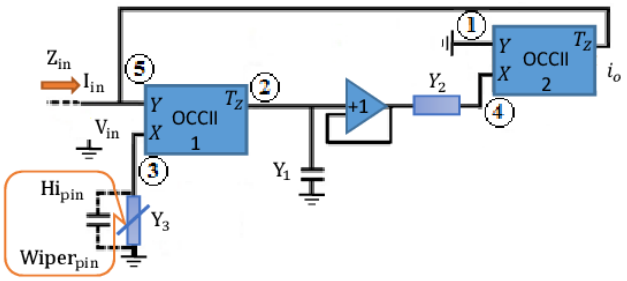

Fig. 5. A schematic of the proposed grounded inductor using two stages of OCCIIs

The corresponding Signal Flow Graph (SFG) of two operational conveyors with three passive components, creating a GIC based on CCII is shown in Fig. 6. In regard to the OCCII behavior, the OCCII-GIC topology can be divided into 3 stages. In the first stage if a voltage is applied to the terminal Y (node5), an equal potential will appear on the input terminal X (node3), while, the input current in node5 is equal to zero (I_{Y5}=0), the current at node I_{X3} (node3) will be mirrored to output terminal T_Z (node2) derived from the admittance attached to the node3 (Y_3). The second stage is the admittance of Y_1 and voltage amplifier with unity gain. In the third stage, the current on node4 derived from the admittance of Y_2 is replicated to node5 again [63].

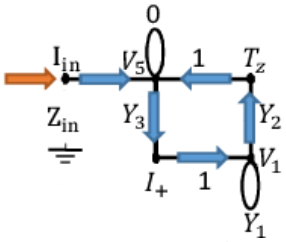

Fig. 6. Shows a Signal Flow Graph (SFG) of the GIC functionality

After simplifying the SFG as indicated in Fig. 6, the following equation (2) for the input impedance function is obtained; if we consider Y_2 and Y_3 as conductance and Y_1 as a capacitance with the current and voltage tracking errors for the non-ideal cases:

$$Z_{in} = \frac{V_{in}}{I_{in}} = \frac{Y_1}{(\alpha_1\alpha_2\beta_1\beta_2)Y_2Y_3} = \frac{sC_1}{\alpha_1\alpha_2\beta_1\beta_2G_2G_3} = sL_{eq} \qquad 2$$

where $\alpha_1, \alpha_2,$ and β_1, β_2 are the current and voltage tracking errors of $OCCII-1$ and $OCCII-2$, respectively. A multi-frequency current source using the stray capacitance cancellation method is developed by utilizing digital-pots to operate as variable resistors, then to produce the variable inductor corresponding to different frequency points (as shown in Fig. 5 with a grounded inductor whereas the conductance Y_3 is a variable resistor). This circuit topology was chosen in attempt to cancel the stray capacitance in the multi-frequency system.

There are limitations to produce a pure inductance in the multi-frequency system because of using a digital-pot. A digital-pot naturally comes with grounded capacitance at both ends (C_H and C_L) and parallel capacitance at the wiper (C_w) as the schematic in Fig. 7 illustrates.

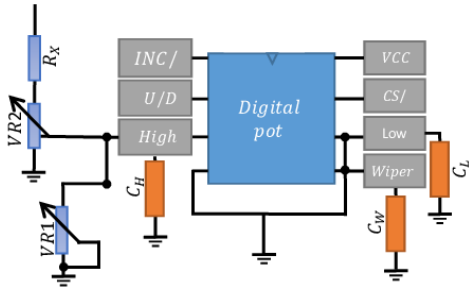

Fig. 7. The diagram shows the DCP schematic circuit and the Trim-pot and digital-pot network as an equivalent circuit for a grounded resistor.

The following equations are computed to consider the action of the OCCII-GIC circuit caused by the digital-pot capacitances, as the digital-pot swings from 1 to the full-scale value to operate in multi-frequency systems, whereas, $Y_1 = sC_1$, $Y_2 = G_2$ and $Y_3 = G_3 + sC_{ground-3}$, we can write:

$$Z_{in} = \frac{V_{in}}{I_{in}} = \frac{Y_1}{(\alpha_1\alpha_2\beta_1\beta_2)\,Y_2Y_3} = \frac{sC_1}{(\alpha_1\alpha_2\beta_1\beta_2)\cdot\ G_2\cdot(G_3+sC_{ground-3})} \qquad 3$$

where,

$$L_{eq} = \frac{sC_1\cdot G_3}{(\alpha_1\alpha_2\beta_1\beta_2)\cdot G_2\cdot(G_3^2+C_{ground-3}^2)} \qquad 4$$

$$R_{eq} = \frac{C_1 \cdot C_3}{(\alpha_1\alpha_2\beta_1\beta_2) \cdot G_2 \cdot (G_3^2 + C_{ground-3}^2)} \quad 5$$

2.5 Implementation of the proposed EIM system

2.5.1 Resistors

In the design of a system with high output impedance, a high priority is given to balance between resistors to achieve full precision output. Resistors with a tolerance of 1% achieve an output impedance maximum of around 250kΩ at low frequency. Therefore, a high resistor matches in current excitation system with precision tolerance of ±0.01%, and TCR ±5ppm/℃ (Stackpole Electronics, Inc. Precision Thin Film Chip Resistor) [64] is utilized to achieve maximum output impedance at a high frequency bandwidth for the case of the EIM system.

2.5.2 Operational Voltage Amplifier (Op Amp)

In order to find the best choice of op amp, first, we compared different op amps in regard to their performance characteristic and EIM application. We consider the noise performance of the inputs and output, within the general category of the op amp, i.e. current and voltage input offsets, voltage stability, voltage shift rail-to-rail and rejection response in the general to select the best op amp. In the next step, we used OrCAD PSpice to simulate op amp circuits and the basic components to find the final choice of the module. Since we need to get the maximum output impedance in a current source, the common-mode rejection ratio (CMRR) of the op amp needs to be optimized, e.g. an op amp with a CMRR of 60dB results in an output impedance of less than 1MΩ. In addition, non-linearity of the CMRR curve in an op amp results in a disadvantage that does not produce a flat output impedance curve (non-linear result). Thus, we used amplifiers with a FET input instead of CMOS or bipolar input.

We selected OPA656 (Texas Instruments) [65], which is built with a JFET input stage to offer an ultra-high dynamic range amplifier with high precision performance. Typical characteristics show that the OPA656 has a high input impedance of $10^{12}||2.8$pF in common-mode and $10^{12}||0.7$pF in differential-mode and low bias current with excellent THD performance of -80dBc at 10MHz and excellent differential gain and differential phase of 0.02% and 0.05° [65]. This is sufficient to provide an ultra-low 7nV/Hz input voltage noise also to achieve a very low integrated noise over a wide bandwidth of 500MHz.

2.5.3 Current conveyor module

We selected an AD844S (ANALOG DEVICES' module) [66] for current feedback with a high-speed Trans-impedance op amp. It combines high bandwidth and very fast large signal response with a settling time of 100ns to 0.1% and essentially independent gain. It shows excellent differential gain and a differential phase of 0.03% and 0.15° with an input capacitance of 2pF and input resistor for inverting input equal to 50Ω and non-inverting input of 10MΩ, Trans-impedance of 4.5pF||3MΩ. The offset voltage β_1 and β_2 are reduced to a few tens of μV and the input resistance is around 50Ω. This module can deliver up to ± 50mA into a 50Ω load with low distortion in regard to voltage ripple of ± 18V. This module also comes with a buffer to produce a unity gain complementary voltage that it uses to drive the low impedance loads. All these typical characteristics make AD844S suitable as a current conveyor module with high bandwidth compared to other existing current conveyor module.

2.5.4 Potentiometer network

The multi-frequency current excitation is delivered by using a digitally controlled potentiometer (DCP) XICOR of X9C102 [67] that is employed in the OCCII-GIC circuit. In fact, the variable resistor is paralleled by a grounded capacitance of C_H=10pF with the wiper and low pins grounded. The DCP includes 99 resistive elements that can be changed in 100 steps (ΔR=10.1010Ω for the case of 1kΩ) combined with two stages of trim-pot network (BOURNS 3269W-102 with 12 turns with a rotational time of 200 cycles) [68] achieves the minimum variable (ΔR) resistor with the smallest capacitance effect.

2.5.5 Drive and Receive multiplexers

The EIM system tested in this study consists of 85 electrodes where the distance between each two electrodes is 17mm. 1,416 independent measurement combinations based on 123 current injection channels are achieved. Using this large number of measurement combinations increases quality (including contrast and SNR) of the reconstructed images. We used a hexagonal structure based on a four-electrode method, where the current injection electrodes are located at the vertices of the hexagonal measurement shape. The hexagonal measurement structure is a novel data acquisition pattern that shows a suitable pattern for the planar electrode plate, with each 19 electrodes forming 3 current injections and is capable of giving 36 measurement combinations by using a 120 degree rotation around the x axis for each pair of electrode injections. The main reason for using this hexagonal pattern is to obtain the best SNR and minimized dynamic range, since the voltage measurements from electrodes outside of this hexagonal pattern have a low SNR. In addition, in planar topology the sensitivity increases from the boundary to the inner area, in contrast to ring topology in which the sensitivity decreases from the boundary to the inner area.

Since the EIM system consists of 85 electrodes, it needs to connect the current excitations and the differential voltage measurement system to the 85 electrodes individually. A cascading multiplexer structure using two-stages of the drive MUXs is designed to reduce the on/off switch capacitance effects in drive MUXs, which are directly involved in the output impedance of the EIM system. It uses ADG1211, iCMOS, Quad with $C_{Off/On} = 0.9\text{pF}, 2.6\text{pF}$, for the 1st stage, and 8 unbuffered analogue switch array modules of ADG2128, CMOS 8×12 with $C_{off/on} = 6\text{pF}, 9.5\text{pF}$ in 2nd stage [69,70]. Therefore, it has been broken the parallel elements of the input (On capacitances) of the drive MUXs. The outcome of the cascade multiplexer topology focuses on some modified key elements to improve system performance by reducing the on/off capacitances of the multiplexers that affect a single channel. As a result, it enables good isolation with a low parasitic capacitance, allowing the multi-channel EIM system to operate over a wide frequency bandwidth. The drive multiplexer uses the cascading method to crop the stray capacitance of 20.8pF involved in each injection channel. We

choose 6 cross-point 16×16 switch matrix modules of ADV3205 with parallel programming and an input buffer array (switch times < 60ns with 0.1% settling time) that connect the electrodes to a single-ended differential amplifier to measure the potential differences across the sample.

2.5.6 Differential Voltage amplifier

The principle that we used in the measurement subsystem is based on injecting the same amount of current into two electrodes that are $180°$ out of phase, thus the voltage difference between the two injecting pads is determined by the impedance of the connecting subject under test. To effectively detect this voltage difference, we need a differential-to-single-ended amplifier with very high CMRR at high frequency. Adjustable gain is also required to measure the two different output voltage signals at different frequencies with the best SNR and without clipping in the circuitry. This is used for converting the differential voltage measurement signals ($V_{IN}+$ and $V_{IN}-$) to a single-ended voltage signal. The AD8130 [71] module with user adjustable gain set is used for amplifying the output signals. The gain is set by the ratio of two resistor values of R_G and R_F, $V_{OUT} = V_{IN}(1+R_f/R_G)$, while, we measured CMRR ratio at different frequencies, regardless of the gain setting as part of calibration method. We compared different structures (modules) and selected the AD8130 module in this EIM system because it had a very high input impedance around -75dBc at 10MHz, stable voltage for both inputs, low distortion and low noise performance.

2.5.7 Control Unit

An addressing control unit (ACU) system is used to control the drive and receive channel selections of the MUXs. The EIM system uses a four-electrode measurement method, with 123 drive electrode combinations per frame. The latency is equal to the sum of all the internal delays and external delays per electrode combination × the number of measurement combinations per frame, which is equal to 1,416 measurement combinations. The control unit of the EIM system is based on an MCU [72] to control and address the drive and receive – MUXs, programmable gain of the voltage measurement (PGA), auto and manual calibration methods. The accurate current excitation and acquisition time depends on all these parts.

The switching of the two stages of drive MUXs is done in tens of microseconds and has little effect on speed. However, other delays may slow down the ADC acquisition process due to the need for filters (resistors and capacitors to ideally remove ripple) in the demodulation of the signal. We wrote software that allows us to set the delay time after setting up the MUXs, and before we are taking an A to D measurement. We used filters in the demodulators that speeds up the process by a factor of 10 when switching in resistors 10 times smaller for 0.5ms, to speed up the charging process and make the output closer to the final value faster. After a 0.5ms wait the ADC reading is taken. This means that using a 100 kHz measurement frequency in similar circuits, the system is able to take a single ADC measurement in 1ms. We used different filters when measurements are performed at different frequencies, so that a frame completed at a high frequency can use a faster filter to eliminate the ripple and the filter capacitor can also charge up faster. Practically at 1MHz, a single ADC measurement is taken in 0.1ms. Thus the data acquisition takes 1416ms (or less than one and half seconds) per frame.

2.5.8 Circuit board

We built a single custom compact planar EIM circuit board in 6 layers with a finished board thickness of 1.76mm. It consists of all analogue subsystems including current excitation systems with a parasitic capacitance cancellation method, two stages of the cascading drive MUXs that directly connected to 2×85 channels on the drive side, a data acquisition system with receive side multiplexers of 85×2 shared between electrodes, one stage buffer voltage amplifier, a PGA and auto and manual calibration circuits with switching control using an MCU. In addition, 85 spring-loaded electrodes are placed between the electrode pad and the breast planar electrode plate without any cables. Fig. 8 shows the bottom and top sides of the custom single compact EIM circuit board. This is exactly compatible with what we mentioned as the structure of the EIM shown in Fig. 1.

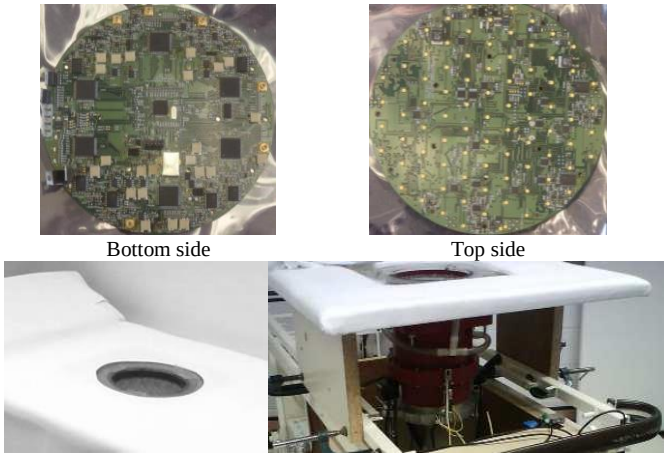

Fig. 8. The Sussex EIM custom single circuit board includes all the analogue subsystems. The figures show the bottom and the top sides and measurement tank 180 mm dia., open top surface, 5mm thick acrylic walls and the clinical bed. An 85 electrode planar plate at the top side of the EIM board is directly connected to a breast immersed in a measurement tank.

3. EXPERIMENTS AND RESULTS

3.1 Current excitation under test

Since the new EIM system was designed and built based on a four-electrode technique [73], it has 123 drives and produces 1,416 measurement combinations per frame. In the experiment, two electrodes that are $180°$ out of phase inject electrical current equally through drive multiplexers into the subject and the other two electrodes measure the voltages, the measurements are repeated at multiple frequencies. Each current branch and voltage measurement node is switched between 85 electrodes. Therefore, two OCCII-GICs are used for the two $180°$ out of phase current branches to compensate the stray capacitance of each branch.

We detected transient output current data from the EIM system with an AC sweep at single and multi-frequencies to demonstrate the behavior of the current excitation system. In practice, the measurement data are obtained with the regarding to three main component specifications as follows: (1) each op amp has an input impedance of the differential of $0.7pF||10^{12}\Omega$

and a common-mode of 2.8pF||$10^{12}\Omega$ with CMRR of the amplifier, (2) the resistor has a tolerance of 0.01%, 25℃ paralleled with a capacitance of 0.3pF that generally is created by a circuit board and (3) the effect of digital-pot capacitance 10pF on the OCCII-GIC circuit for the grounded variable resistor in Y_3 admittance, and the current source and Trans-conductance gains. In the experiment to test this multi-frequency EIM system, we also followed the tuning process step by step. This obtains the maximum output impedance corresponding to the stray capacitance of the circuit design for each frequency point. It is necessary to adjust the OCCII-GIC corresponding to the stray capacitance in each branch for each frequency point. A large output impedance was achieved by making the above adjustments.

The AC sweep and Transient analysis results of the multi-frequency system up to 3 MHz were measured and plotted in Fig. 9 (a)–(c). Although the output capacitance was not fully removed and caused the appearance of a phase shift in the output current signal as shown in Fig. 9 (c), we were able to use calibration methods to cancel the effect of phase shift based on hardware and IR software [17]. However, the output impedance found with an AC analysis does not take into consideration the effect of the rail voltage of the circuits used. The input drive voltage of the AC constant current generator must be reduced in order to use this principle to measure the output impedance. In reality, we need to consider the input drive in order to avoiding output clipping in the current excitation circuits.

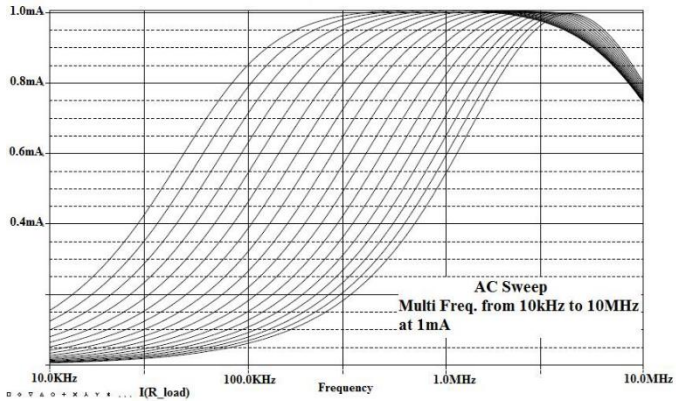

(a)

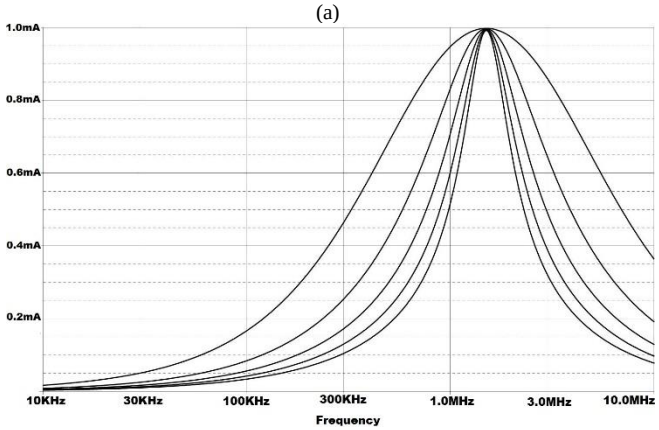

(b)

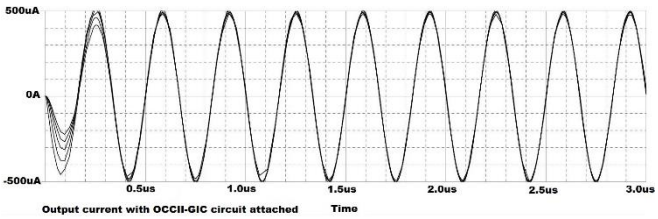

(c)

Fig. 9. (a)A multi-frequency AC sweep output of the new current excitation system with the frequency increment of 200 kHz from 1MHz to 3MHz. Digital-pot Y_3 (100Ω to 5kΩ, increment in 10 logarithmic steps per decade). (b) The AC sweep output at a frequency sample point of 1.5MHz with different loads from 1kΩ to 5kΩ (c) The transient output current analysis of the current excitation system at the single frequency sample around 3MHz as an example frequency point for the variable load with 0.5mA^{pp}.

3.2 Measuring the output impedance of the current excitation under test

The full EIM output impedance including the current excitation under test and a capacitance cancelling circuit has been treated with the parallel combination of a total output resistance and capacitance ($Z_O = R_O||Z_{C_O}$). When the current excitation system delivers electrical current into a load, Z_O needs to be large with respect to the load in order not to affect the measurements unduly. This means R_O and Z_{C_O} need to be large with respect to the load at all frequency points. Therefore, at low frequencies the impedance of R_O is the main effect on the AC voltage on the load impedance and at high frequencies $Z_{C_O} = \frac{1}{j\omega C_O}$ must be large with respect to the load impedance, thus, C_O must be small. In our experiment, a near perfect 1MΩ resistor was made by using two in series 0.5 MΩ ±0.01% tolerance resistors. They are suspended in air. Thus, it reduces the parallel stray capacitance to an estimated small value of 0.1pF across the pair as load resistance.

In this experiment, two different approaches were applied to measure output impedance Z_O as shown in Fig. 10 (a). *1st test structure*, earth the input and measure the output voltage when the output is driven by an AC current source. *2nd test structure*, drive the input with a voltage using the fact that the circuit delivers a constant current dependent on the input voltage. This confirms correctly the transfer ratio of 1V/mA when the phase error is small. Therefore, in this test the only load on the output is Z_O. So we can measure the output voltage and deduce C_O. Alternatively we added a known load R_O and deduced C_O where C_O is in parallel with R_O as shown in Fig. 10 (b). In this case, the output impedance (Z_O) is found by considering the output impedance in parallel with this load.

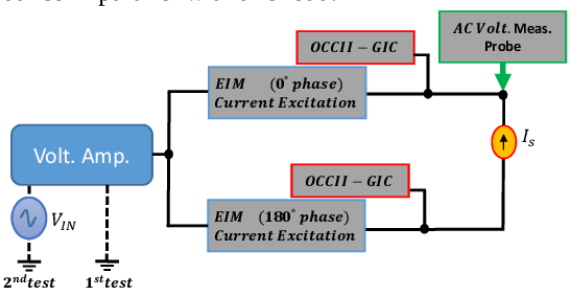

(a)

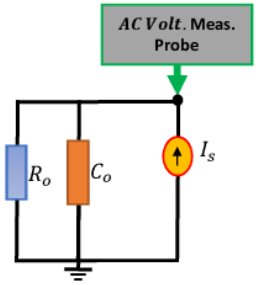

(b)

Fig. 10. (a) A perfect current source connected to the output point of the current excitation and measuring the AC voltage, where in 1st test is grounded then in the 2nd test used a Vin=1V as a input voltage to obtain 1mA output current (b) a perfect AC current source with output resistance (R_O) and output capacitance (C_O) and measuring the AC voltage to obtain equivalent value of the output impedance.

For the first method, we set the input drive to zero, injected 1mA electrical current generated from a perfect AC current source into the output point and measured the amplitude and phase of the output. This presents a characteristic shape when the output voltage amplitude and phase are recorded and plotted against frequency. Then to find the output resistance and capacitance from the output signal, we drive with an identical perfect AC source a parallel earthed resistor, R_{EXP}, and capacitor, C_{EXP} and change the R_{EXP} and C_{EXP} values until the shapes of the amplitude and phase plots match. If a load impedance was used to bring the output near 0V, the output impedance was found by considering the output impedance in parallel with this load. We used an AC source, and probes with suitable high output impedance, $>10^{11}\Omega$ and <0.1fF, and high frequency, >10MHz for taking the practical measurements.

To validate the performance of the current source, a plot of the output impedance versus frequency is provided as shown in Fig. 11 (a). We assign the resulting maximum values of R_O and Z_O when minimizing the output capacitance C_O of the circuit. The output impedance is influenced by the digital-pot in the OCCII-GIC, so that we used an auto-tuning system to achieve the maximum output impedance of the excitation system to eliminate the total output capacitance to <7fF. As a result, output impedances of 10MΩ at 1MHz to at least 3MΩ at 3MHz frequency point were achieved. Although a phase shift is present in the output signals as shown in Fig. 11 (b), therefore it computed and split from the measurement data.

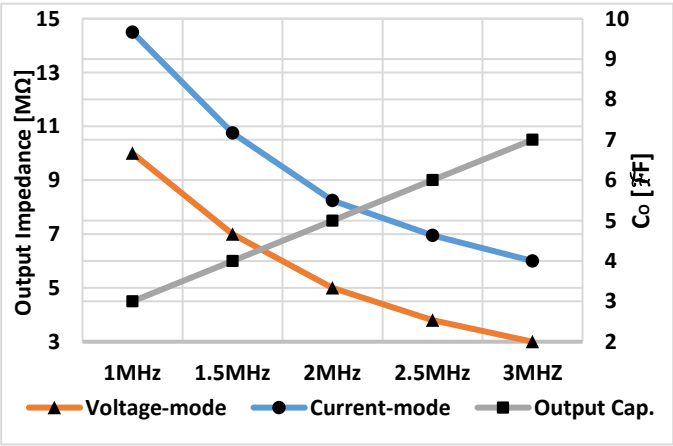

(a)

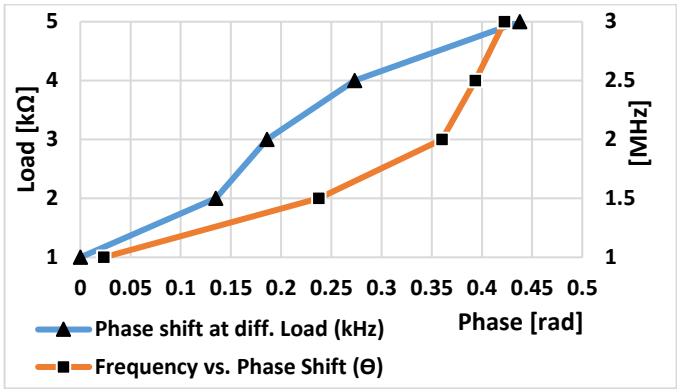

(b)

Fig. 11. (a) A result of the output impedance (Z_O) when cancelling unwanted capacitive effects of the EIM system over the frequency range of 1MHz to 3 MHz, (b) Phase responses measured over frequency range of 1 MHz - 3 MHz and phase responses measured over a load range of 1kΩ – 5kΩ.

3.3 *Phantom based Experiments*

System instabilities can be caused by the EIM design and must be characterized before and during the clinical trials. To characterize and assess the newly designed EIM system and test the improvement of SNR and/or the accuracy of impedance measurements, we especially designed a realistic electronic phantom (E-phantom) for this new EIM system. This mesh phantom provides predictable, stable, and reproducible signals. The mesh phantom is based on the electrode configuration and mesh structures of the image reconstruction. This includes the effect of the complex impedance model of tissues using a distributed complex circuit of the extra-cellular resistance R, resistance of intracellular tissue S and the membrane capacitance properties C (RSC circuit tissue model).

We connected the EIM system directly to the E-phantom by using 85 spring-loaded electrodes with less than 20mΩ [74] for plug-in connection. Three RSC tissue circuit models of fat, stroma tissues, and carcinoma are inserted into the E-phantom [39] as target tissues in three different locations. The different RSC values are used, which were selected based on the impedivity of breast tissue reported in [26,75,76] and the assumption that the breast tissue has the dimensions of 10mm×10mm×10mm in a cubic shape to reconstruct electrical impedance images in the planar structure at multi-frequency as shown in Fig 12. This also presents dynamic information to assess the performance of the EIM system to simulate *in vivo* conditions.

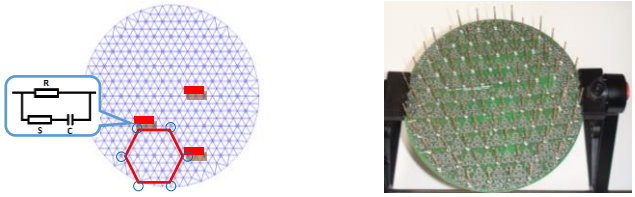

(a) Planar E-phantom

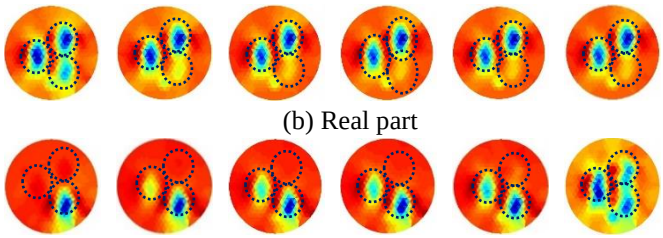

(b) Real part

(c) Imaginary part

Fig. 12. (a) Planar E-phantom with an 85 electrode array using hexagonal pattern. (b) and (c) A result of the EIM image using an E-Phantom over the frequency range of 10 kHz to 3MHz within three RSC models of fat (at 9 o'clock), stroma (at 2 o'clock) and carcinoma (at 5 o'clock).

The total data set composes of 123 current injections producing 1,416 measurement combinations. This measurement was repeated for 100 times and the data analyzed statistically to measure SNR and accuracy. We measured SNR and accuracy for the different measurement indexes, which increased from 1 to 1,416. The results showed that the average SNR of 82.28dB with a maximum SNR of 91.06dB and a minimum SNR of 76.42dB was achieved. In addition, the average modelling accuracy of 99.47% with a maximum and minimum range of 99.97 and 99.91 was achieved.

4. DISCUSSION

Although EIM have been proposed and tested as a potentially promising imaging modality to help improve breast cancer screening and detection of early breast cancer, its clinical utility is limited due to the low SNR of the produced EIM images or impedance maps. Thus, in order to more sensitively or accurately detect abnormal electrical impedance signal variations that have high risk of leading to have or developing breast cancer, the first important task is to improve system design and increase the SNR of the impedance measurements. In this study, we designed, assembled and tested a new unique EIM system with a planar 85 electrodes. The new EIM system has the following unique characteristics.

First, when using an EIM system in a breast cancer screening or prescreening modality, a current excitation implemented and used in an EIM system needs to produce a stable and constant electrical current over a wide range of frequency bandwidth with different loads due to the large variation of breast size and tissue density. This means it needs to have a constant trans-conductance applying to the testing load (subject under test) across the frequency range being tested and scanned. Our new system yields high stable current outputs, because of improvements in the system design such as considering the system noise, power supply noise (low noisy rail voltages) and improving the shielding systems when considering all the individual effects in the system design.

Experimentally the goal was to try to make the circuit give a maximum output impedance at high frequencies with minimum phase shift and gain characteristics. Therefore, in regard to current source performance at high frequency, the effect of the decrease of output resistance and increase of capacitance of the current source (parasitic capacitances especially when multiplexers are used to route the current to electrodes) reduce the total output impedance of the current source. This degrades the ability to produce a good spatial resolution. Our findings confirm that using an unwanted capacitance cancelation method has advantages in achieving a higher output impedance. In order to do this, a gyrator based on an active current conveyor structure (i.e. OCCII-GIC circuit) used in parallel with a current source circuit when the gyrator circuit is tuned for each frequency point. In addition, the excitation system utilizes two OCCII-GIC circuits combined with two 180 degrees out of phase current sources as a mirror structure. Each OCCII-GIC circuit produces a variable inductance in parallel with the RC circuit created by each branch of the current source. Therefore, we need to balance both OCCII-GIC circuits at a desired frequency point in order to minimize phase shift and increase the output impedance of the current excitation system.

Although, conventional GICs composed of two op amps and five passive components have already been proposed as a solution in EIT systems but it does not have an ideal performance for multi-frequency EIT systems. Since the combination of five passive impedance matching (combination of resistance and capacitance components) and two non-ideal op amps should be considered, thus, it will become impractical for a multi-frequency system. On the other hand, our findings confirm that OCCII-GIC circuit based on active components is a similar method to conventional GIC to cancel the stray capacitance but it achieves much better results and works over a higher frequency range. In addition, our results suggest that conditioning the current source of the multi-frequency EIM system based on using the OCCII-GIC circuit to cancel unwanted capacitance effects for improving spatial resolution of the impedance images is a valuable approach. The results showed that it delivered a multi-frequency EIM system based on tunable frequency points with acceptable output impedance for different loads. Since the new EIM system has been tested and achieved a high SNR and modelling accuracy of the transfer impedance measurements.

We built an EIM system based on a planar 85-electrode channel and using an MCU for addressing control between 85 electrodes. We also designed a cascade method for DRV MUXs which consists of 8 parallel DRV MUX modules of 8*12 switch array combined with a pre-stage ultra-low on/off capacitance to avoid on-capacitance parallelism of the drive multiplexers. Therefore, the on/off capacitance of the switching channel becomes very low for each current injection branch, thus increasing the operating frequency and frame rate of the system when comparing it with other existing single-source EIT systems. We used a single-source method compared to semi/fully parallel source methods that use more than one source for a group of channels. This aids in reducing the capacitance effect of DRV MUXs. But this unique cascading method, benefits both reducing these capacitance effects and taking advantage of the single-source structure giving more convenience in the calibration process and repeatability and reproducibility.

Since, most EIT systems use cables or connector boards to inject current and/or to collect measurement data; while our EIM system is a planar structure with a single board, it consists of current injection, electrode plate and voltage measurement systems that are able to inject the current signals and measure the voltage signals with minimum noise. We used an 85 planar electrode plate, which was placed on the bottom of the cylindrical measurement volume. The 85 electrodes fitted on the PCB as a circular in 180mm dia. in order to achieve close electrode contact to the current source and minimize the noise and stray capacitance of the system. Therefore, the performance of the system is not dependent on the type and length of any cables, influence of connector boards, or electrode placement effects.

5. CONCLUSION

The new EIM system is a planar 85 electrode board with multi-frequency channels consisting of two independent current and voltage-based structures. It is designed to operate over a narrow frequency range from 10 kHz up to 3MHz with a high output impedance. The EIM system has been implemented with the OCCII-GIC as a stray capacitance cancellation method improving the system performance and increasing the frequency bandwidth of the system. The performance of the OCCII-GIC has been computed with phase and magnitude errors. This capacitance cancellation technique is capable of working with other existing EIT systems as an enhanced method for multi-frequency systems. This is a significant change in the design compared to the conventional GIC methods used to ameliorate the constraints caused by passive components and op amp limitations. EIM has been implemented for a clinical application that has been tested in the instrumentation and sensor laboratory at the University of Sussex.

6. ACKNOWLEDGMENT

This work is supported in part by an Innovation grant, University of Sussex, England. The authors would also like to acknowledge the support from the Peggy and Charles Stephenson Cancer Center, University of Oklahoma, OK, US.

Reference List

[1] T.K. Bera, N. Jampana, G. Lubineau, A LabVIEW-based electrical bioimpedance spectroscopic data interpreter (LEBISDI) for biological tissue impedance analysis and equivalent circuit modelling, Journal of Electrical Bioimpedance. (2016).

[2] J.R. Macdonald, E. Barsoukov, Impedance spectroscopy: theory, experiment, and applications, History. 1 (2005).

[3] T.K. Bera, Bioelectrical impedance methods for noninvasive health monitoring: a review, Journal of medical engineering. 2014 (2014).

[4] B. Schullcke, B. Gong, S. Krueger- Ziolek, M. Tawhai, A. Adler, U. Mueller- Lisse, K. Moeller, Lobe based image reconstruction in Electrical Impedance Tomography, Med. Phys. 44 (2017) 426-436.

[5] T.K. Bera, J. Nagaraju, G. Lubineau, Electrical impedance spectroscopy (EIS)-based evaluation of biological tissue phantoms to study multifrequency electrical impedance tomography (Mf-EIT) systems, Journal of Visualization. 19 (2016) 691-713.

[6] S. Gloning, K. Pieper, M. Zoellner, A. Meyer-Lindenberg, Electrical impedance tomography for lung ventilation monitoring of the dog, Tierärztliche Praxis Kleintiere. 45 (2017) 15-21.

[7] R. Pethig, Dielectric properties of body tissues, Clinical Physics and Physiological Measurement. 8 (1987) 5.

[8] B. Singh, C. Smith, R. Hughes, In vivo dielectric spectrometer, Medical and Biological Engineering and Computing. 17 (1979) 45-60.

[9] L. Sha, E.R. Ward, B. Stroy, A review of dielectric properties of normal and malignant breast tissue, (2002) 457-462.

[10] D. Barber, B. Brown, Applied potential tomography, Journal of Physics E: Scientific Instruments. 17 (1984) 723.

[11] D.S. Holder, Electrical Impedance Tomography: Methods, History and Applications, first ed., Institute of Physics Publishing, Bristol, 2005.

[12] M. Assenheimer, O. Laver-Moskovitz, D. Malonek, D. Manor, U. Nahaliel, R. Nitzan, A. Saad, The T-SCANTM technology: electrical impedance as a diagnostic tool for breast cancer detection, Physiol. Meas. 22 (2001) 1.

[13] Y. Zou, Z. Guo, A review of electrical impedance techniques for breast cancer detection, Med. Eng. Phys. 25 (2003) 79-90.

[14] W. Wang, B. Tunstall, D. Chauhan, M. McCormick, The design of De Montfort Mk2 electrical impedance mammography system, 2 (1998) 1042-1043.

[15] V. Cherepenin, A. Karpov, A. Korjenevsky, V. Kornienko, A. Mazaletskaya, D. Mazourov, D. Meister, A 3D electrical impedance tomography (EIT) system for breast cancer detection, Physiol. Meas. 22 (2001) 9.

[16] O. Trokhanova, M. Okhapkin, A. Korjenevsky, Dual-frequency electrical impedance mammography for the diagnosis of non-malignant breast disease, Physiol. Meas. 29 (2008) S331.

[17] Xiaolin Zhang, Wei Wang, G. Sze, D. Barber, C. Chatwin, An Image Reconstruction Algorithm for 3-D Electrical Impedance Mammography, Medical Imaging, IEEE Transactions on. 33 (2014) 2223-2241.

[18] A. Hartov, R.A. Mazzarese, F.R. Reiss, T.E. Kerner, K.S. Osterman, D.B. Williams, K.D. Paulsen, A multichannel continuously selectable multifrequency electrical impedance spectroscopy measurement system, Biomedical Engineering, IEEE Transactions on. 47 (2000) 49-58.

[19] R. Halter, A. Hartov, K.D. Paulsen, Design and implementation of a high frequency electrical impedance tomography system, Physiol. Meas. 25 (2004) 379.

[20] A.M. Soliman, Synthesis of Generalized Impedance Converter and Inverter Circuits Using NAM Expansion, in: Anonymous Analog/RF and Mixed-Signal Circuit Systematic Design, Springer, 2013, pp. 223-242.

[21] B. Brown, Electrical impedance tomography (EIT): a review, J. Med. Eng. Technol. 27 (2003) 97-108.

[22] R. Bayford, Bioimpedance tomography (electrical impedance tomography), Annu. Rev. Biomed. Eng. 8 (2006) 63-91.

[23] S. Gabriel, R. Lau, C. Gabriel, The dielectric properties of biological tissues: III. Parametric models for the dielectric spectrum of tissues, Phys. Med. Biol. 41 (1996) 2271.

[24] S. Gabriel, R. Lau, C. Gabriel, The dielectric properties of biological tissues: II. Measurements in the frequency range 10 Hz to 20 GHz, Phys. Med. Biol. 41 (1996) 2251.

[25] A.J. Grodzinsky, Electromechanical and physicochemical properties of connective tissue, Crit. Rev. Biomed. Eng. 9 (1983) 133-199.

[26] A.J. Surowiec, S.S. Stuchly, J.R. Barr, A. Swarup, Dielectric properties of breast carcinoma and the surrounding tissues, Biomedical Engineering, IEEE Transactions on. 35 (1988) 257-263.

[27] C. Gabriel, A. Peyman, E. Grant, Electrical conductivity of tissue at frequencies below 1 MHz, Phys. Med. Biol. 54 (2009) 4863.

[28] K.S. Cole, R.H. Cole, Dispersion and absorption in dielectrics I. Alternating current characteristics, J. Chem. Phys. 9 (1941) 341-351.

[29] J.J.B. Jack, D. Noble, R.W. Tsien, Electric Current Flow in Excitable Cells, Clarendon Press Oxford, 1975.

[30] T.I. Oh, H. Wi, D.Y. Kim, P.J. Yoo, E.J. Woo, A fully parallel multi-frequency EIT system with flexible electrode configuration: KHU Mark2, Physiol. Meas. 32 (2011) 835.

[31] A.S. Ross, An adaptive current tomograph for breast cancer detection, Ph.D. dissertation, (2003a).

[32] A. Wilson, P. Milnes, A. Waterworth, R. Smallwood, B. Brown, Mk3. 5: a modular, multi-frequency successor to the Mk3a EIS/EIT system, Physiol. Meas. 22 (2001) 49.

[33] A. McEwan, G. Cusick, D. Holder, A review of errors in multi-frequency EIT instrumentation, Physiol. Meas. 28 (2007) S197.
[34] A. McEwan, A. Romsauerova, R. Yerworth, L. Horesh, R. Bayford, D. Holder, Design and calibration of a compact multi-frequency EIT system for acute stroke imaging, Physiol. Meas. 27 (2006) S199.
[35] W. Wang, B. Tunstall, D. Chauhan, M. McCormick, The design of De Montfort Mk2 electrical impedance mammography system, 2 (1998) 1042-1043.
[36] H. Gagnon, M. Cousineau, A. Adler, A.E. Hartinger, A resistive mesh phantom for assessing the performance of EIT systems, Biomedical Engineering, IEEE Transactions on. 57 (2010) 2257-2266.
[37] H. Griffiths, A phantom for electrical impedance tomography, Clinical Physics and Physiological Measurement. 9 (1988) 15.
[38] T.K. Bera, J. Nagaraju, A chicken tissue phantom for studying an electrical impedance tomography (EIT) system suitable for clinical imaging, Sensing and Imaging: An International Journal. 12 (2011) 95-116.
[39] A. Zarafshani, T. Qureshi, T. Bach, C.R. Chatwin, M. Soleimani, A 3D Multi-frequency response electrical mesh phantom for validation of the planar structure EIT system performance, (2016) 0600-0604.
[40] P. Crawley, G. Roberts, High-swing MOS current mirror with arbitrarily high output resistance, Electron. Lett. 28 (1992) 361-363.
[41] R.A. Pease, A comprehensive study of the Howland current pump, National Semiconductor. January. 29 (2008).
[42] W. Wang, M. Brien, D. Gu, J. Yang, A comprehensive study on current source circuits, (2007a) 213-216.
[43] A. Mahnam, H. Yazdanian, M.M. Samani, Comprehensive study of Howland circuit with non-ideal components to design high performance current pumps, Measurement. 82 (2016) 94-104.
[44] D. Bouchaala, O. Kanoun, N. Derbel, High accurate and wideband current excitation for bioimpedance health monitoring systems, Measurement. 79 (2016) 339-348.
[45] D.H. Sheingold, Impedance & admittance transformations using operational amplifiers, Lightning Empiricist. 12 (1964) 7.
[46] R. Bragos, J. Rosell, P. Riu, A wide-band AC-coupled current source for electrical impedance tomography, Physiol. Meas. 15 (1994) A91.
[47] O. Casas, J. Rosell, R. Bragós, A. Lozano, P. Riu, A parallel broadband real-time system for electrical impedance tomography, Physiol. Meas. 17 (1996) A1.
[48] F. Seoane, R. Bragós, K. Lindecrantz, P. Riu, Current source design for electrical bioimpedance spectroscopy, In: Encyclopedia of Healthcare Information Systems. (2008) 359-367.
[49] K. Smith, A. Sedra, The current conveyor—A new circuit building block, Proc IEEE. 56 (1968) 1368-1369.
[50] J. Robinson, New CCII current conveyor, Application Notes. 4198 (2008) 1Y6.
[51] P. Eloranta, Current Conveyors, History, Theory, Applications and Implementation, Postgraduate Course in Electronic Circuit Design II, Helsinki University of Technology. (2004).
[52] A. Sedra, K.C. Smith, A second-generation current conveyor and its applications, IEEE Transactions on Circuit Theory. 17 (1970) 132-134.
[53] A.S. Sedra, P.O. Brackett, Filter Theory and Design: Active and Passive, Matrix Pub, 1978.
[54] P. Bowron, F.W. Stephenson, Active Filters for Communications and Instrumentation, McGraw-Hill, 1979.
[55] S. Franco, Design with Operational Amplifiers and Analog Integrated Circuits, 4th ed., McGraw-Hill, New York, USA, 2014.
[56] D.R. Muñoz, S.C. Berga, C.R. Escrivá, Current loop generated from a generalized impedance converter: a new sensor signal conditioning circuit, Rev. Sci. Instrum. 76 (2005) 066103.
[57] I.A. Khan, M.H. Zaidi, A novel generalized impedance converter using single second generation current conveyor, Active and passive electronic components. 26 (2003) 91-94.
[58] B. Maundy, S. Gift, P. Aronhime, Realization of a GIC using hybrid current conveyor/operational amplifier circuits, (2007) 163-166.
[59] S.J. Gift, New simulated inductor using operational conveyors, International journal of electronics. 91 (2004) 477-483.
[60] M.T. Abuelma'Atti, Comment on'Active simulation of grounded inductors with CCII s and grounded passive elements', International journal of electronics. 87 (2000) 177-181.
[61] M.O. Cicekoglu, Active simulation of grounded inductors with CCII s and grounded passive elements, International Journal of Electronics. 85 (1998) 455-462.
[62] S. Prakobnoppakao, B. Chipipop, W. Surakampontorn, K. Watanabe, Design of a Current-Mode CCII-Based Bandpass Filter from Immittance Function Simulator using Commercial Available CCII (AD844), (2002) 743-746.
[63] D. Biolek, Novel signal flow graphs of current conveyors, Circuits and Systems, 1995. , Proceedings. , Proceedings of the 38th Midwest Symposium on. 2 (1995) 1058-1061 vol.2.
[64] Data Sheet-Resistive Product, Precision Thin Film Chip Resistor, tolerances to ±0.01%, RNCF Series (2015).
[65] Data Sheet-OPA656, Operational Amplifier, Wideband, Unity Gain Stable FET-Input, SBOS196G, (2008) 25.
[66] Data Sheet-AD844S, Current Conveyor, Monolithic Op Amp, 60 MHz, 2000 V/ms, with Current Feedback Amplifiers, REV. C (2009) 20.
[67] Data Sheet-X9C102, E2POT Nonvolatile Digital Potentiometer, 3863-2.4 2/12/99 T2/C0/D0 SH (1996).
[68] Data Sheet-3269W, 3269 - 1/4 ” Square SMD Trimpot, Trimming Potentiometer, Trimpot (2011).
[69] Data Sheet-ADG1211, Analog Switches Multiplexers, Low Capacitance, Low Charge Injection, iCMOS, Quad SPST Switches, Rev. B (2012a) 16.
[70] Data Sheet-ADG2128, Analog Switches Multiplexers, I^2C CMOS, 8 X 12 Analog Switch Array with Dual/Single Supplies, Rev. D (2012b) 28.
[71] Data Sheet-AD8130, Voltage Measurement, Low Cost, 270 MHz Differential Receiver Amplifier, Rev. C (2005b) 40.
[72] Data Sheet-PIC18F87K90, Family, 64/80-Pin, High-Performance Microcontrollers with LCD Driver and nanoWatt XLP Technology, DS39957B (2010).
[73] H.P. Schwan, Detection of Biological Impedances, Physiological Techniques in Biological Research, New York Academic Press, 1963.
[74] DATA SHEET-INGUN, INGUN GKS-100 224 130A 2000E, Test Probes, Catalog 2003/04 (2004).
[75] J. Jossinet, The impedivity of freshly excised human breast tissue, Physiol. Meas. 19 (1998) 61.
[76] J. Jossinet, M. Schmitt, A review of parameters for the bioelectrical characterization of breast tissue, Ann. N. Y. Acad. Sci. 873 (1999) 30-41.